PLOS Computational Biology

RESEARCH ARTICLE

Cooperative molecular interaction networks govern PARP1 inhibitor selectivity and binding affinity

Alejandro Feito[1,2], Natàlia DeMoya-Valenzuela[3], Cristian Privat[3], Andrés R. Tejedor[1,2,4], Lucía Paniagua-Herranz[3], Adiran Garaizar[5], Alberto Ocana[3,6]*, Jorge R. Espinosa[1,2,4,6]*

1 Department of Physical Chemistry, Universidad Complutense de Madrid, Madrid, Spain, **2** Instituto Pluridisciplinar, Universidad Complutense de Madrid, Madrid, Spain, **3** Experimental Therapeutics Unit, Hospital Clínico San Carlos (HCSC), Instituto de Investigación Sanitaria San Carlos (IdISSC), Madrid, Spain, **4** Yusuf Hamied Department of Chemistry, University of Cambridge, United Kingdom, **5** Data Science, Bayer AG, Monheim am Rhein, Germany, **6** PhAsIca Biosciences S.L, Madrid, Spain

* alberto.ocana@salud.madrid.org (AO); jorgerene@ucm.es (JRE)

OPEN ACCESS

Citation: Feito A, DeMoya-Valenzuela N, Privat C, R Tejedor A, Paniagua-Herranz L, Garaizar A, et al. (2026) Cooperative molecular interaction networks govern PARP1 inhibitor selectivity and binding affinity. PLoS Comput Biol 22(5): e1014296. https://doi.org/10.1371/journal.pcbi.1014296

Editor: Dirk Walther, Max Planck Institute of Molecular Plant Physiology: Max-Planck-Institut fur molekulare Pflanzenphysiologie, GERMANY

Received: January 16, 2026

Accepted: May 5, 2026

Published: May 26, 2026

Data availability statement: We provide the relevant data in the repository (https://github.com/Reshiiiii/PARP_Data_Scripts) to facilitate reproducibility of our results. In the repository

Abstract

Selective inhibition of PARP1 represents a promising strategy to improve the therapeutic index of PARP inhibitors, a class of anticancer agents that exploit defects in DNA repair pathways. While PARP inhibitors have shown remarkable clinical benefit, particularly in BRCA-mutated tumors, the lack of discrimination between PARP1 and its close homolog PARP2, often leads to hematological toxicity and limits treatment efficacy. Thus, achieving molecular selectivity for PARP1 remains a central challenge in the rational design of safer and more potent inhibitors. To explore the molecular determinants of ligand selectivity, we focus on four clinically relevant PARP inhibitors—two PARP1-selective (saruparib and NMS-P118) and two non-selective (veliparib and olaparib) inhibitors—and perform atomistic potential-of-mean-force calculations of the PARP1 catalytic binding domain in the presence of these molecules. Our simulations near-quantitatively capture the experimental relative binding preferences, demonstrating that our approach reliably reflects selectivity patterns. Based on these findings, we analyze protein–ligand contact frequencies to identify the stabilizing interaction network and contact connectivity inducing protein selectivity. The most frequent protein–inhibitor contacts are primarily mediated by tyrosine triads and electrostatic interactions, showing a cooperative complex network of intermolecular contacts which strongly relies on protein multivalency. To dissect the decisive role of individual residues across the binding site, we also perform targeted mutagenesis of the PARP1 catalytic pocket in complex with saruparib, replacing several active-site amino acids by glycines. Progressively increasing the number of mutations markedly reduces binding stability, with distinct residue combinations exerting two primary effects: destabilization of the final bound state and the emergence of energetic barriers along the ligand association pathway. Together, our results provide a coherent

we also give the necessary code to run the simulations and accessible instructions to obtain our results.

Funding: A. F. acknowledges funding from the Ramon y Cajal fellowship (RYC2021-030937-I) and Spanish National Grant (PID2022-136919NA-C33). A. R. T. acknowledges funding from the Juan de la Cierva fellowship (JDC2024-053759-I). J. R. E. acknowledges funding from Emmanuel College, the University of Cambridge, the Ramon y Cajal fellowship (RYC2021-030937-I), the Spanish scientific plan and committee for research reference PID2022-136919NA-C33, and the European Research Council (ERC) under the European Union's Horizon Europe research and innovation program (grant agreement no. 101160499). A.O., N.D.-V., C.P. and L.P.-H. acknowledge funding from CRIS Cancer Foundation (AOF.C01CRIS and AOF.M01CRIS). The funders had no role in study design, data collection and analysis, decision to publish, or preparation of the manuscript.

Competing interests: I have read the journal's policy and the authors of this manuscript have the following competing interests: J.R.E. and A.O. are co-founders of PhAsIca Biosciences S.L. The authors declare that this relationship does not affect the design, analysis, or conclusions of this work. All other authors declare no competing financial interests. Other authors declare that they have no known competing financial interests or personal relationships that could have appeared to influence the work reported in this paper.

mechanistic framework for understanding PARP1 selectivity and informs the rational design of next-generation inhibitors with improved efficacy and safety.

Author summary

Poly(ADP-ribose) polymerase (PARP) inhibitors are widely used anticancer drugs that target DNA repair mechanisms, particularly in tumors with BRCA mutations. However, most current inhibitors lack specificity and target both PARP1 and PARP2, which can lead to toxic side effects and limit their clinical benefit. In this study, we investigate the molecular basis of selective PARP1 inhibition, a key step toward designing safer and more effective therapies. Using advanced molecular simulations, we analyze how four clinically relevant inhibitors—two selective and two non-selective—interact with the PARP1 catalytic domain. Our results accurately reproduce experimental binding preferences and reveal that selectivity arises from a cooperative network of interactions, dominated by aromatic residues and electrostatic contacts. These interactions form a multivalent binding environment that stabilizes selective inhibitors more effectively. Additionally, by introducing targeted mutations in the binding site, we demonstrate how specific amino acids contribute to both binding strength and the pathway by which inhibitors associate with the protein. Overall, our findings provide a detailed mechanistic understanding of PARP1 selectivity and offer valuable insights for the rational design of improved anticancer drugs.

1 Introduction

Poly(ADP-ribose) polymerase 1 (PARP1) and 2 (PARP2) are nuclear enzymes that play essential roles in the detection and repair of DNA damage [1,2], particularly single-strand breaks [3]. Acting as central guardians of genomic integrity, these enzymes orchestrate coordinated responses to DNA lesions that ensure efficient repair [2], preserve chromatin organization [2] and maintain cellular viability [4]. Upon sensing DNA damage, PARP1—responsible for the majority of damage-induced PARylation—and the related enzyme PARP2 catalyze the polymerization of poly(ADP-ribose) chains, thereby recruiting nuclear factors that promote chromatin remodeling [5–7] and the assembly of DNA repair complexes [8]. Beyond their canonical roles in DNA repair, PARP1 and PARP2 contribute to transcriptional regulation [9], replication fork stability [10], and cellular responses to oxidative stress [11], underscoring their broad involvement in nuclear homeostasis. Defects in these pathways—such as those associated with *BRCA1/2* mutations [12,13]—are tightly linked to oncogenesis [14–18]. Therefore, the central role of PARP1, and to a lesser extent PARP2, in DNA damage sensing and repair makes them compelling therapeutic targets, particularly in tumors dependent on compensatory repair mechanisms for survival [19,20].

Targeting PARP1 with small-molecule inhibitors has become an effective therapeutic strategy [15,21–23], exploiting synthetic lethality in cancers with homologous recombination (HR) repair deficiency [24,25]. Clinically approved PARP inhibitors—including olaparib [26–28], rucaparib [29,30], niraparib [31,32], and talazoparib [33,34]—inhibit both PARP1 and PARP2. This lack of selectivity contributes to a narrow therapeutic window and characteristic hematologic toxicities largely attributed to PARP2 inhibition [14,28,35]. Next-generation inhibitors such as saruparib [36] or NMS-P118 [37] were designed to achieve greater PARP1 selectivity, thus minimizing adverse hematologic effects [38] and emphasizing the clinical importance of selectively targeting PARP1 [18]. Developing highly specific PARP inhibitors not only promises improved tolerability but also enables rational combination therapies with additional DNA-damaging agents under a safer therapeutic profile [39]. Both saruparib and NMS-P118 were conceived as PARP1-selective inhibitors, but their clinical outcomes differ: NMS-P118 displayed approximately 150-fold selectivity over PARP2 and remained preclinical [37], with its development primarily supported by biochemical characterization and efficacy in preclinical tumor models, while saruparib exhibited up to 500-fold selectivity [40], enhanced hematologic safety, and has advanced to clinical trials [41], where its pharmacological profile has translated into favourable tolerability and measurable antitumor activity in patients, showing durable responses in HR-deficient tumors [18]. Thus, beyond differences in PARP1/PARP2 selectivity, the two compounds also differ in their stage of development and the level of clinical evidence currently available.

Understanding the molecular basis of inhibitor selectivity requires mechanistic knowledge of how these ligands interact with specific amino acid residues within the catalytic binding site, as well as with accessory factors such as HPF1 [42,43], which modulate enzymatic activity [18,44–46]. Although high-resolution structural data provide essential configurations of these interactions, they often fail to capture the conformational dynamics and solvent effects which are critical for predicting binding affinity and specificity [47,48]. Atomistic molecular dynamics (MD) simulations [49–53] can successfully address these limitations by describing inhibitor binding at the atomistic level in an explicitly solvated medium and within a dynamically evolving environment under physiological conditions. By characterizing the conformational flexibility of the active site, identifying key protein-ligand contacts, and quantifying binding energy landscapes [54], MD simulations bridge static structural information with the dynamic behavior of biomolecular systems. Unlike crystallographic models, these simulations incorporate solvent, ions, and conformational ensembles, producing a realistic description of ligand–protein recognition. Such computational framework enables the dissection of the energetic and structural determinants underlying potency and selectivity, allowing systematic testing of hypotheses which are often inaccessible experimentally. In this way, MD simulations not only guide rational drug design and optimization of existing inhibitors, but can also accelerate the discovery of new compounds with improved efficacy and safety.

In this study, we perform atomistic MD simulations of PARP1 and PARP2 catalytic binding domains in complex with a representative set of inhibitors, including PARP1-selective compounds (NMS-P118 [37] and saruparib [36]) and non-selective inhibitors (olaparib [26] and veliparib [26,55]). The binding free energy is evaluated via potential-of-mean-force (PMF) calculations, while residue-level protein-ligand contacts within the catalytic binding site are analyzed and compared with available experimental data. To connect bound-state interactions with ligand binding strength, we further perform targeted *in silico* mutagenesis by replacing selected active-site amino acids by glycines, with particular emphasis on the interactions driving selectivity in saruparib. Together, our results integrate structural, energetic, and residue-level analyses to elucidate the molecular determinants of PARP1 selectivity, providing a mechanistic framework for the rational design of more potent and specific PARP1 inhibitors.

2 Results

2.1 Potential of mean force calculations to quantify PARP–ligand interactions: Insights into the binding mechanisms and ligand selectivity

To quantify the strength of ligand-protein binding interactions and to characterize the energetic pathway underlying ligand association within the active site, we perform PMF calculations using Umbrella Sampling simulations [56–59]

and the all-atom a99SB-*disp* force field with the TIP4P-*disp* water model [60,61] under physiological conditions (310 K, 150 mM NaCl; see Sections SI and SII of the S1 Appendix for further methodological details). This force field are specifically designed to provide an accurate balance between protein–protein, protein–water, and solvation interactions, which is essential for reliably describing conformational flexibility and ligand binding processes in biomolecular systems. The force field parameters and topology for all ligands are derived using the OpenFF toolkit [62], ensuring full compatibility with the all-atom parameters of the protein sequence using the a99SB-*disp* force field (see Section SI of the S1 Appendix for further computational details). Unlike static structural analysis, this approach allows us to explicitly probe the free energy landscape governing the association and dissociation pathways of the different inhibitors. PMF simulations provide a quantitative description of the free energy profile along a defined reaction coordinate, chosen here as the center-of-mass (COM) distance between the inhibitor and the catalytic binding pocket. This enables direct monitoring of how the interaction energy evolves as the ligand approaches or moves away from the protein binding site (see Section SI in the S1 Appendix for simulation details of this method). Our PMF initial configurations are build from crystallographically resolved protein–ligand complexes available in the Protein Data Bank (see Section SII of the S1 Appendix for PDB codes used in this study), with the exception of the PARP2–saruparib system, for which no experimental structure is available. For this system, the initial bound configuration is generated through molecular docking structural alignment into the corresponding PARP2 pocket [63]. From these initial configurations for each PARP1/PARP2-ligand complex, we generate a series of protein–ligand subsequent configurations separated by incremental COM distances and ensuring overlap along the reaction coordinate, defining different Umbrella Sampling windows. For each window, we perform independent simulations subsequently combined to reconstruct the PMF profile as a function of the protein–ligand COM distance (Fig 1A). The resulting PMF profiles exhibit a pronounced free energy minimum near the crystallographic binding distance, corresponding to the most stable bound configuration. As the ligand is progressively displaced from the binding site, the free energy increases and eventually plateaus near zero, indicating complete dissociation and the absence of effective protein–ligand intermolecular interactions beyond such distance (see Fig 1A for a schematic representation of a ligand-protein PMF profile).

In Fig 1B–1C, we present the PMF profiles for NMS-P118 and olaparib, respectively, including the corresponding curves for PARP1 and PARP2. The PMF for NMS-P118-PARP1 (orange curve; Fig 1B) exhibits a deep energy minimum of approximately -16.6 kcal/mol, indicative of high binding affinity. The energy landscape is relatively flat, showing significantly low desolvation energy barriers at intermediate distances (1–2 Å). In contrast, the PMF for PARP2 (violet curve) reveals a markedly weaker binding affinity, with a shallow minimum of only -4.1 kcal/mol. Notably, this profile features a moderate energy barrier of approximately 3 kcal/mol at intermediate distances (~0.8 Å) that is absent in PARP1. Such barrier possibly reflects unfavorable desolvation effects and the energetic cost of displacing water molecules solvating NMS-P118 prior to the formation of energetically favorable ligand–protein interactions, thereby hindering the association of NMS-P118 with PARP2. Although the final bound state remains moderately favorable, the combination of a weak minimum for PARP2 and a much higher binding free energy for PARP1 explains the experimentally established selectivity of NMS-P118 for PARP1 [37,64]. For olaparib (Fig 1C), the PMF profile for PARP1 (red curve) shows an energy minimum of -17.8 kcal/mol, while PARP2 (blue curve) exhibits a similarly deep minimum of -18.1 kcal/mol. Both curves gradually descend along the reaction coordinate, indicating low to moderate energy barriers and an overall smooth association pathway. Notably, the PARP2 curve displays a subtle local minimum at intermediate distances, suggesting transient interactions that may guide the ligand toward the active site and facilitate binding. The comparable depths of the energy wells in both protein pockets provide a clear mechanistic explanation for the lack of selectivity of olaparib, consistent with experimental measurements [65]. The same calculations are also performed for both saruparib and veliparib (Fig A of the S1 Appendix), and the depth of the global minimum for each PMF profile is reported in Fig 1D.

Our results are broadly consistent with experimental observations: both saruparib and NMS-P118 exhibit a markedly higher binding affinity for PARP1, veliparib shows a modest preference for PARP1 [66,67], while olaparib is generally

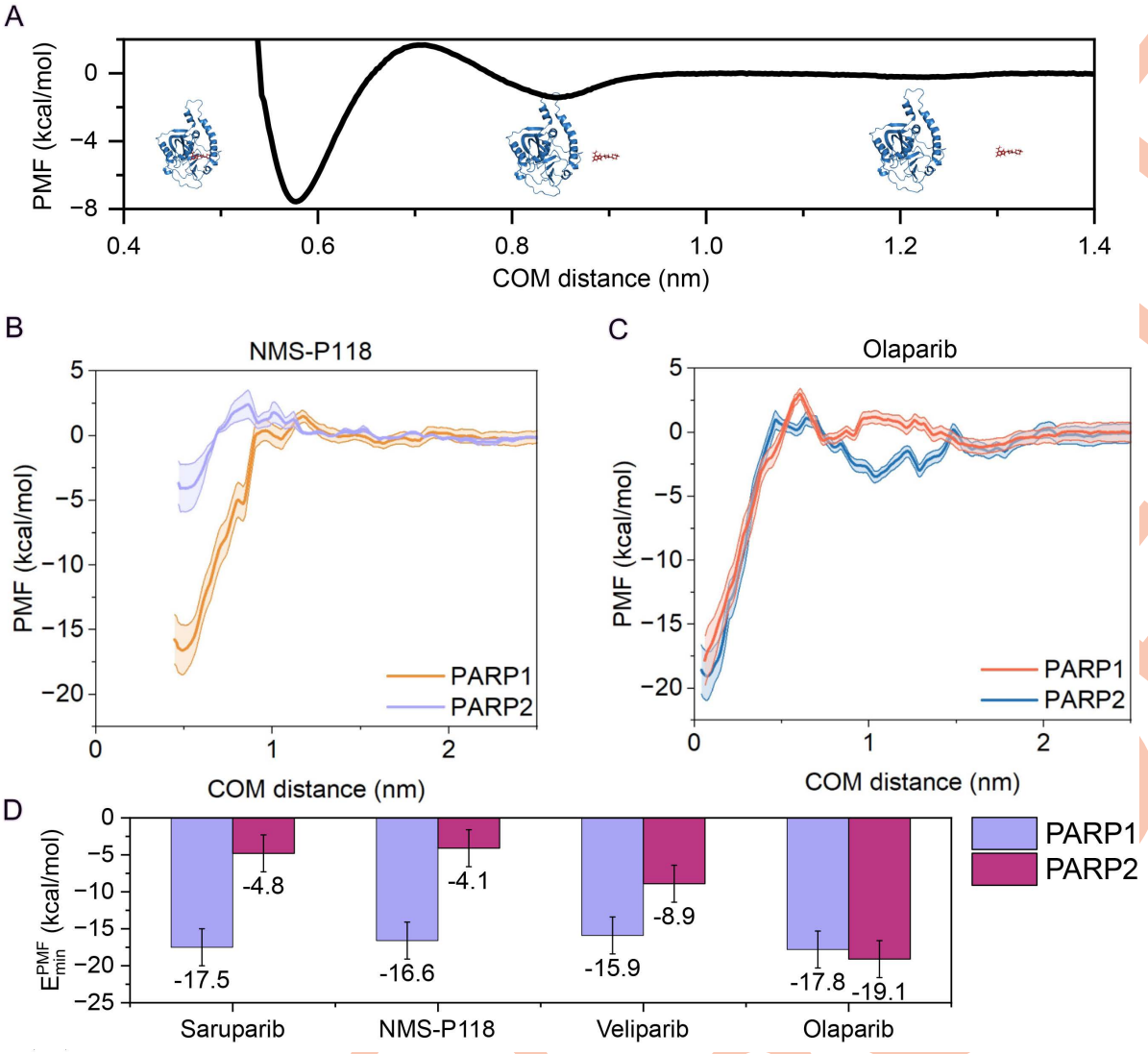

Fig 1. (A) Schematic representation of a PMF profile between the protein and the ligand as a function of the distance of the center-of-mass (COM). Inset show representative configurations taken at different protein–ligand distances along the reaction coordinate (COM distance). **(B–C)** Atomistic PMF dissociation profiles between each ligand and PARP1/PARP2 under physiological NaCl concentration (150 mM) and room conditions, in explicit solvent and ions. The COM distance between the protein binding pocket and the ligand is used as the reaction coordinate. Curves are shown for NMS-P118 (B) and olaparib **(C)**, depicting the statistical uncertainty of each PMF profile by a color shadowing corresponding to the standard deviation obtained from trajectory segments (see Section SI of the S1 Appendix for further details). **(D)** Summary of the free energy minima obtained through PMF calculations for all ligands in complex with PARP1 (violet) and PARP2 (maroon).

https://doi.org/10.1371/journal.pcbi.1014296.g001

considered non-selective [67,68] (Fig 1D). Measurements of the half maximal inhibitory concentration, IC_{50}, indicate that both veliparib and olaparib only show limited PARP1 selectivity and, in certain contexts, even a relative preference for PARP2 [64,65,67,69–71]. We provide a direct comparison between the binding free energy values (ΔG) obtained from our PMF profiles and those experimentally derived from IC_{50} values using the following relation [72]:

$$\Delta G_{binding} = RT\ln(IC_{50}(M)) \quad (1)$$

where R is the gas constant, and $T = 300$ K. Experimental IC_{50} values were taken as follows: saruparib, 3 nM for PARP1 (closed blue symbol) and 1400 nM for PARP2 (open blue) [40]; NMS-P118, 9 nM for PARP1 (closed red) and 1390 nM for PARP2 (open red) [37]; veliparib, 8.3 nM for PARP1 (closed green) and 11 nM for PARP2 (open green) [70]; and olaparib, 1.1 nM for PARP1 (closed orange) and 0.9 nM for PARP2 (open orange) [73] and then converted into binding ΔG values. In Fig 2, the experimentally derived ΔG values are compared with those extracted from the PMF profiles, revealing a qualitative correlation across the data set. We note that the absolute free energies quantitatively differ: experimental values of ΔG range approximately from –8 to –13 kcal mol^{-1}, whereas the PMF minima span from about –20 to –5 kcal mol^{-1}. This discrepancy likely arises from several potential sources: (1) inherent limitations of the employed force field [60]; (2) the positional restraints applied during the PMF calculations which constrain the ligand conformational freedom and may thus overstabilize the binding interaction strength in all systems [58,74]; (3) the choice of the reaction coordinate for the dissociation pathway along the PMF calculations; and (4) the reduction of the dissociation pathway to a single reaction coordinate in the PMF calculations, which may introduce systematic errors due to the projection of a multidimensional free-energy landscape onto one dimension. As illustrated in Fig N in the S1 Appendix, where the PMF profiles of the PARP1–saruparib complex calculated in one and three dimensions are compared, the three-dimensional treatment provides a free-energy value that quantitatively approaches the experimental reference. This comparison highlights the inherent approximations associated with the one-dimensional description. Finally, part of the discrepancy may originate from the experimental reference itself, as IC_{50} values do not directly report equilibrium binding affinities, but instead reflect inhibitory potency under specific assay conditions. Thus, converting them into binding free energies involves an approximation that neglects condition-dependent effects and experimental variability, potentially contributing to deviations in the absolute ΔG values. All these factors introduce a systematic offset that cannot be precisely quantified. Therefore, the error bars in Fig 2 reflect only the statistical uncertainty of our PMF calculations. Nevertheless, despite these sources of uncertainty and our systematic offset (which would affect all systems equally), our simulations near-quantitatively reproduce the experimentally reported selectivity for these ligands. Overall, the relative binding preferences between PARP1 and PARP2 are consistently captured, confirming that our PMF-based approach reliably recapitulates the experimental selectivity patterns. A similar trend to that shown in Fig 2 can also be observed in Fig B of the S1 Appendix, which

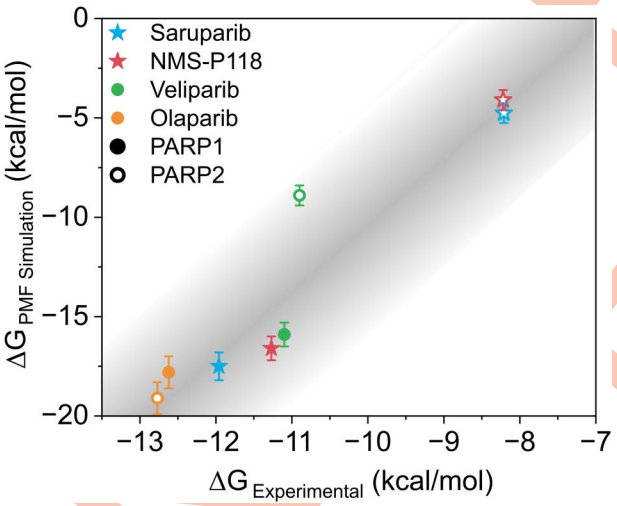

Fig 2. Comparison between experimental ($\Delta G_{Experimental}$) and simulated ($\Delta G_{PMF\ Simulation}$) binding free energies for different inhibitors (Saruparib, NMS-P118, Veliparib, and Olaparib) for PARP1 (closed symbols) and PARP2 (empty symbols). Specific inhibitors of PARP1 are plotted in stars and non-specific inhibitors in circles. A linear shading to the obtained correlation was added as a guide to the eye.

https://doi.org/10.1371/journal.pcbi.1014296.g002

compares the differences in $\Delta G_{binding}$ between PARP1 and PARP2 for both experimentally and computationally-derived free energies.

2.2 Residue-level contact analysis of PARP inhibitors

Understanding atomic-level interactions between small-molecule inhibitors and the active site of PARP1 *vs.* PARP2 is essential to elucidate the molecular basis of selectivity. Consequently, we analyze the molecular contact network between the selected ligands and the catalytic site of both enzymes obtained from 1 microsecond trajectories (see Section SIII of the S1 Appendix for further details). We select two PARP1-specific inhibitors (NMS-P118 [37] and saruparib [36]) and two non-selective inhibitors (olaparib [26] and veliparib [26,55]) to assess whether the resulting contact profiles can provide insight into ligand selectivity. For each inhibitor, we compute the number of contacts between each heavy atom of the ligand and the center of mass of the side chain of each amino acid. A contact is defined to occur when that distance is less than 6 Å(see Section SIII of the S1 Appendix for methodological details). Such threshold is chosen to capture specific non-covalent interactions while ensuring meaningful intermolecular binding [75] (see Fig C of the S1 Appendix for further detailed protein–ligand contact frequency maps). The number of contacts per heavy atom is normalized by the highest frequency for each ligand to allow comparison of the relative distribution of contacts across all inhibitors studied for both PARP1 (Fig 3A–3D) and PARP2 (Fig 3E–3H). Consequently, the relative contact score, ranging from 0 to 100 (%), is represented on a rainbow color scale. A summary of the most relevant protein residues which contact each ligand is provided in Fig 3I for PARP1 and Fig 3J for PARP2. In particular, only interactions that persisted over 80% of the total simulation time are included, ensuring that the reported contacts are both stable and functionally relevant.

In Fig 3A, we present the normalized contact frequency of NMS-P118 within the catalytic binding pocket of PARP1. The atoms exhibiting the highest contact frequency are located within the fluorinated aromatic group (C2–C1–C4) and the amide moiety (C6–O28–N19). The fluorinated ring predominantly interacts with LYS903, consistent with the positive charge of the lysine side chain. The amide moiety also engages in multiple polar interactions with SER904, HIS862, and GLY863. Moreover, NMS-P118 forms $\pi-\pi$ stacking interactions with several tyrosine residues (TYR889, TYR896, and TYR907), which likely contribute to the ligand's residence time within the active site and to the cooperative stabilization of the contact network governing its binding affinity. Notably, residues HIS862, GLY863, TYR889, TYR896, ALA898, LYS903, SER904, and TYR907 maintained contacts for more than 80% of the total simulation time (see Fig 3I), in agreement with static X-ray crystallographic structures of the corresponding ligand–protein complexes [37]. This consistency supports the contact network predictions derived from our MD simulations.

The contact frequency analysis between PARP1 and saruparib is shown in Fig 3B. In this case, the region of the ligand exhibiting the highest frequency of contacts is centered around the aromatic ring at the lower part of the molecule (C12–C16 and N3). The most frequent and persistent interactions within the catalytic pocket involve the same residues observed for NMS-P118—namely HIS862, GLY863, ALA898, LYS903, SER904, TYR896, and TYR907—suggesting a conserved binding mode driven by a shared network of key non-bonded interactions despite the structural differences among both ligands (see Fig 3I). The tail region of saruparib displays non-bonded interaction modes between the amino groups of the non-aromatic ring and the residue side chains of ASP766 and ASP770. Moreover, the terminal amide group (centered on C17) engages in strong electrostatic interactions with ARG878, further stabilizing the ligand within the binding pocket. Importantly, the interactions identified from our simulations are consistent with those observed in X-ray crystallographic structures—ASP770, HIS862, GLY863, ARG878, ILE879, SER904, and TYR907—of the PARP1–saruparib complex [36]. Furthermore, our simulations reveal some transient additional contacts arising from the intrinsic flexibility of both the protein and the ligand, such as ASP776, LEU769, ALA880, PRO881, TYR896, ALA898, LYS903 and GLU988, which are not reported in static crystallographic configurations.

In Fig 3C, we present the interaction profile between olaparib and the catalytic domain of PARP1. The overall contact pattern closely resembles that of saruparib, reflecting the structural similarities between the two molecules, including

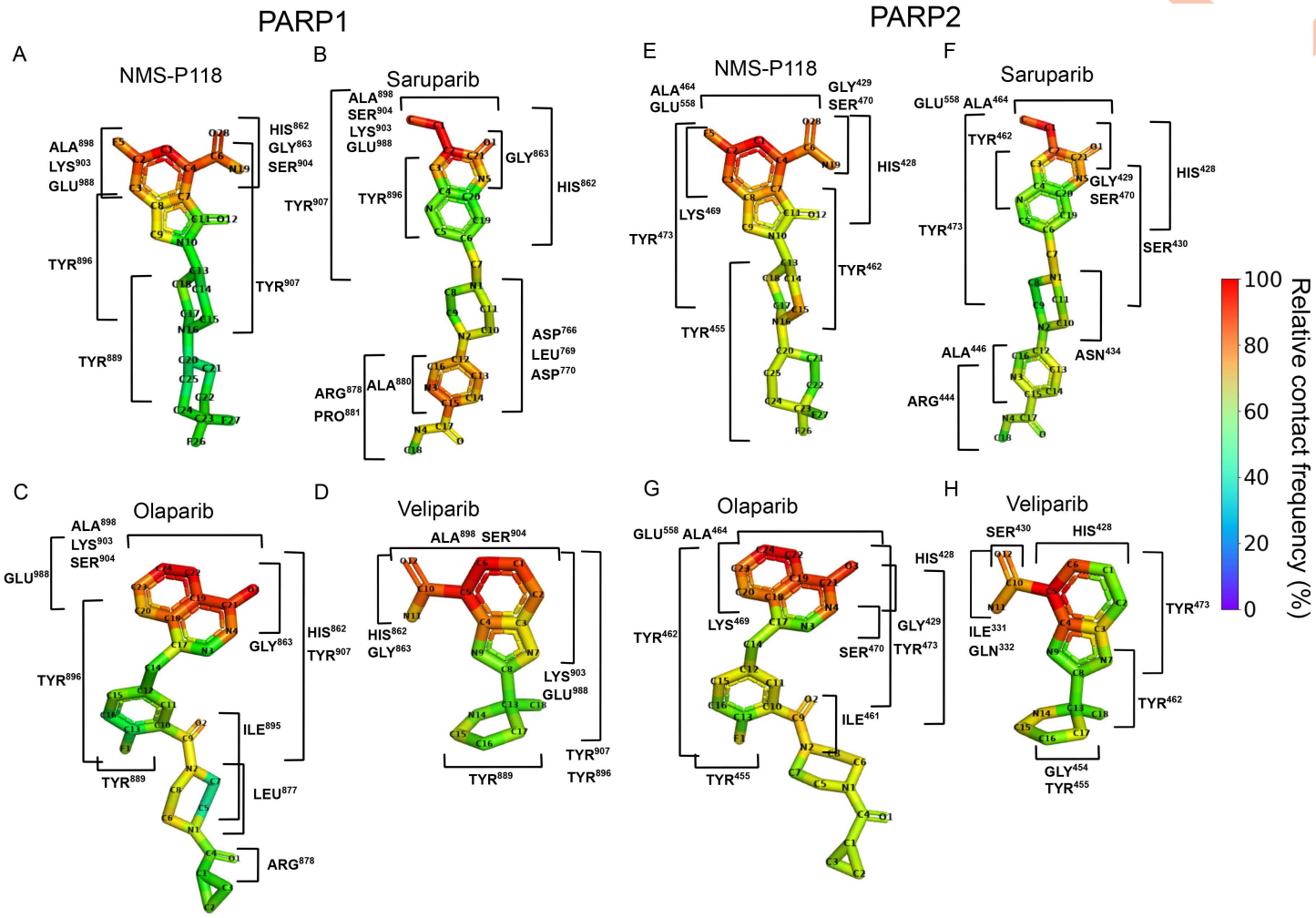

I

PARP1	NMS-P118	Saruparib	Olaparib	Veliparib
RC in all inhibitors	HIS^{862}, GLY^{863}, TYR^{896}, ALA^{898}, LYS^{903}, SER^{904}, TYR^{907}, GLU^{988}			
Common RC in different inhibitors	TYR^{889}		TYR^{889}	TYR^{889}
		ARG^{878}	ARG^{878}	
Specific RC of each inhibitor		ASP^{766}, LEU^{769}, ASP^{770}, ALA^{880}, PRO^{881}	LEU^{877}, ILE^{895}	

J

PARP2	NMS-P118	Saruparib	Olaparib	Veliparib
RC in all inhibitors	HIS^{428}, TYR^{462}, TYR^{473}			
Common RC in different inhibitors	TYR^{455}		TYR^{455}	TYR^{455}
		SER^{430}	SER^{430}	SER^{430}
	GLY^{429}, ALA^{464}, LYS^{469}, SER^{470}, GLU^{558}	GLY^{429}, ALA^{464}, LYS^{469}, SER^{470}, GLU^{558}	GLY^{429}, ALA^{464}, LYS^{469}, SER^{470}, GLU^{558}	
Specific RC of each inhibitor		ASN^{434}, ARG^{444}, ALA^{446}	ILE^{461}	ILE^{331}, GLN^{332}, GLY^{454}

High contact frequency Medium contact frequency Low contact frequency

Fig 3. Relative contact frequency (%) of the PARP inhibitors with PARP1 (saruparib (A), NMS-P118 (B), olaparib (C), and veliparib (D)) and with PARP2 (saruparib (E), NMS-P118 (F), olaparib (G), and veliparib (H)) within the corresponding catalytic binding site. The relative contact frequency was calculated as the number of contacts per heavy atom, normalized by the highest value for each ligand-protein complex. Key protein residues contacting (RC) the different inhibitors forming complexes with PARP1 (I) and PARP2 **(J)**. Residues are colored according to the number of heavy-atom contacts established with the ligand: red indicates residues forming more than six contacts, orange corresponds to residues forming three to six contacts, and green highlights those forming one to three contacts. Rows indicate residue categories: contact residues present in all complexes, common residues among different inhibitors, and specific residue contacts of each inhibitor.

https://doi.org/10.1371/journal.pcbi.1014296.g003

their shared interaction with ARG878 (see Fig 3I and Fig 3A,3C), but with considerably lower frequency in olaparib, hinting a potential mode of selectivity. Moreover, olaparib displays specific interactions including $\pi-\pi$ stacking interaction with TYR889 through its fluorinated aromatic ring (C12–C13–F1), similar to that observed for NMS-P118 but with lower persistence (see the second row in Fig 3I). Interestingly, LEU877 and ILE895 emerge as unique contacts for olaparib, promoting its binding through non-polar interactions specific to its chemical structure. Although X-ray crystallography has resolved several of the key interactions between PARP1 and olaparib—particularly those involving catalytic residues [26] (GLY863 and TYR907)—our atomistic MD simulations provide an extended comprehensive depiction of the binding interface including additional interactions such as HIS862, TYR889, ALA898, TYR896, LYS903, SER904, and GLU988.

Finally, the contact profile between veliparib and PARP1 is given in Fig 3D. The binding mode of veliparib is characterized by extensive $\pi-\pi$ stacking interactions involving the aromatic residues TYR889, TYR896, and TYR907, distributed along a significant region of the ligand due to its smaller molecular size compared to the other inhibitors. Additionally, our results reveal that the most frequent contacts are concentrated around the core of the ligand (i.e., the bicyclic aromatic rings, C1–C6, and the C10-centered amide), corresponding to its most reactive region. The persistent nature of these core interactions, together with the distributed $\pi-\pi$ stacking, likely enhances the overall affinity, and anchors veliparib within the active site.

Similarly, in Fig 3E–3H we present the contact analysis between PARP2 and the different inhibitors: NMS-P118 (E), saruparib (F), olaparib (G), and veliparib (H). Overall, the interaction profiles resemble those observed for PARP1, involving comparable types of non-covalent contacts with homologous aromatic and polar residues within the binding pocket. Notably, when focusing on selective ligands (i.e., NMS-P118 and saruparib), their interaction distributions appear more homogeneous in PARP2. This effect likely reflects intrinsic differences in the binding interface, which in PARP2 are slightly more extended and permissive compared to PARP1, thereby enabling milder interactions with the specific regions of the ligands. For all PARP2–ligand complexes except for NMS-P118, the maximum contact frequency is lower than in their corresponding PARP1 complexes. However, in the case of NMS-P118, a broader contact distribution is maintained, suggesting genuine structural differences in ligand engagement that may contribute to the binding selectivity. In saruparib, the contacts involving the pyridinecarboxamide moiety—less buried within the active site—are markedly reduced in PARP2 compared to PARP1. Thus, while these four inhibitors display broadly similar binding modes between PARP1 and PARP2 at the residue identity level, the observed variations in contact distribution, absolute frequency, and spatial inter-connectivity indicate a crucial role of the contacts for ligand recognition, with selectivity arising from subtle energetic differences in how these interaction networks are organized between both proteins.

Analogously, Fig 3I lists the residues that consistently interact with all inhibitors in complex with PARP2. In contrast to PARP1, only a limited set of residues—specifically HIS428, TYR462, and TYR473—form common contacts across all ligands, suggesting a more restricted conserved interaction core within the PARP2 binding pocket at the level of residue identity. As with the PARP1 analysis, grouping the ligands according to their PARP1 selectivity does not reveal nitid contact patterns at the level of individual residue identity that are exclusive to either selective or non-selective compounds. Nonetheless, certain trends emerge within different subgroups. For instance, NMS-P118 and the non-selective inhibitors all interact with TYR455, while saruparib and the non-selective compounds share contacts with SER430, although with different binding probabilities. Interestingly, a broader set of shared contacts is observed between the PARP1-selective inhibitors and olaparib, including residues such as GLY429, ALA464, LYS469, SER470, and GLU558. This overlap suggests that olaparib may partially mimic the interaction profile and contact connectivity of PARP1-selective inhibitors within PARP2, potentially explaining its relatively balanced affinity for both protein paralogs. In general, our contact analysis captures ligand-specific patterns in residue interactions and binding poses, which together with the PMF free energy analyses provide a comprehensive view of the molecular determinants of PARP1 selectivity.

2.3 Binding interaction analysis of PARP inhibitors

To further characterize the nature of the protein–ligand interactions, we next carry out a per-residue binding energy decomposition for PARP1, aimed at identifying the dominant stabilizing forces and comparing how different inhibitors engage the catalytic pocket. This analysis resolves the specific energetic contributions from van der Waals (vdW), electrostatic (El), and solvation terms, the latter separated into polar solvent (PS) and non-polar solvent (NPS) components, providing a quantitative description of the energetic basis underlying inhibitor binding. The decomposition is carried out using the Molecular Mechanics/Poisson-Boltzmann Surface Area (MM/PBSA) approach (see Section IV of the S1 Appendix for further technical details). Our results are summarized in Fig 4, which depicts both the spatial distribution of key energetic contributors mapped onto the protein surface (left panels) and the residue-specific energy components (right panels).

For the NMS-P118-PARP1 complex (Fig 4A), the strongest contributions arise from the aromatic residues TYR889, TYR896, and TYR907, primarily through van der Waals interactions, complemented by electrostatic stabilization from HIS862, GLY863, and GLU988. LYS903 also contributes through polar solvation effects that help secure the ligand within the catalytic site. In the olaparib-PARP1 complex (Fig 4B), the same tyrosine triad (TYR889, TYR896, TYR907) again dominates, although additional stabilization arises from ARG847 and GLU988, reflecting the distinct geometry of the olaparib scaffold. Saruparib (Fig 4C) engages the same canonical tyrosine residues, but a broader network of interactions is observed, with ASP766, ASN767, and LEU769 also providing stabilizing contributions, consistent with its extended contact surface within the binding pocket. Finally, veliparib (Fig 4D) maintains the general pattern of tyrosine-centered van der Waals stabilization, while electrostatic contributions from HIS862 and polar solvation effects from LYS903 are comparatively more pronounced, balancing its overall energetic signature. Across all complexes, van der Waals interactions consistently constitute the dominant stabilizing contribution, supported by residue-specific electrostatic contributions and, to a lesser extent, by polar solvation. In contrast, non-polar solvation contributions are marginal in multiple cases, with values generally close to the threshold of 1 kcal/mol. This relatively uniform energetic profile suggests that, within the resolution of the MM/PBSA framework, PARP1–ligand binding is predominantly stabilized by van der Waals and electrostatic interactions, as well as by localized polar contacts, whereas non-polar solvation contributions appear comparatively negligible. Nevertheless, subtle differences in residue-level contributions—such as the broader stabilization network in saruparib or the enhanced polar solvation terms in veliparib—highlight how small variations in chemical structure can fine-tune the energetic landscape of ligand binding.

The same binding free energy decomposition is performed for PARP2 (see Fig D in S1 Appendix). The average binding energies for all inhibitors are shown in Fig EA in S1 Appendix and Fig FA in S1 Appendix for PARP1 and PARP2 respectively, while the residue-level energetic contributions are detailed in Fig EB-D in S1 Appendix and Fig FB-D in S1 Appendix. Our analysis indicates that the overall energetic landscapes of PARP1 and PARP2 are alike at the level of residue-resolved MM/PBSA decomposition. In both proteins, the dominant stabilizing forces arise from van der Waals interactions, primarily mediated by the conserved tyrosine triad (TYR889, TYR896, and TYR907 in PARP1; TYR462, TYR473, and TYR455 in PARP2), together with secondary contributions from HIS862, GLY863, and GLU988 (HIS428, GLY429, and GLU558 in PARP2). Polar solvation terms associated with LYS903 (LYS469 in PARP2) also provide measurable stabilization, whereas non-polar solvation contributions remain marginal in all cases. When comparing distinct inhibitors, no pronounced differences are detected in the average interaction energies or in the residue-specific decomposition profiles within the statistical resolution of the MM/PBSA analysis (Fig E in S1 Appendix and Fig F in S1 Appendix), or in the hydrogen bond analysis (Fig G in S1 Appendix). Both selective and non-selective inhibitors engage a largely overlapping set of residues with broadly comparable energetic contributions, and the relative weighting between van der Waals and electrostatic components remains similar across ligands at this level of analysis. This outcome suggests that residue-level binding free energy analysis through MM/PBSA, while highly informative for identifying residues that stabilize the complex, might be insufficient by itself to fully resolve the molecular origin of binding selectivity between closely related paralogs.

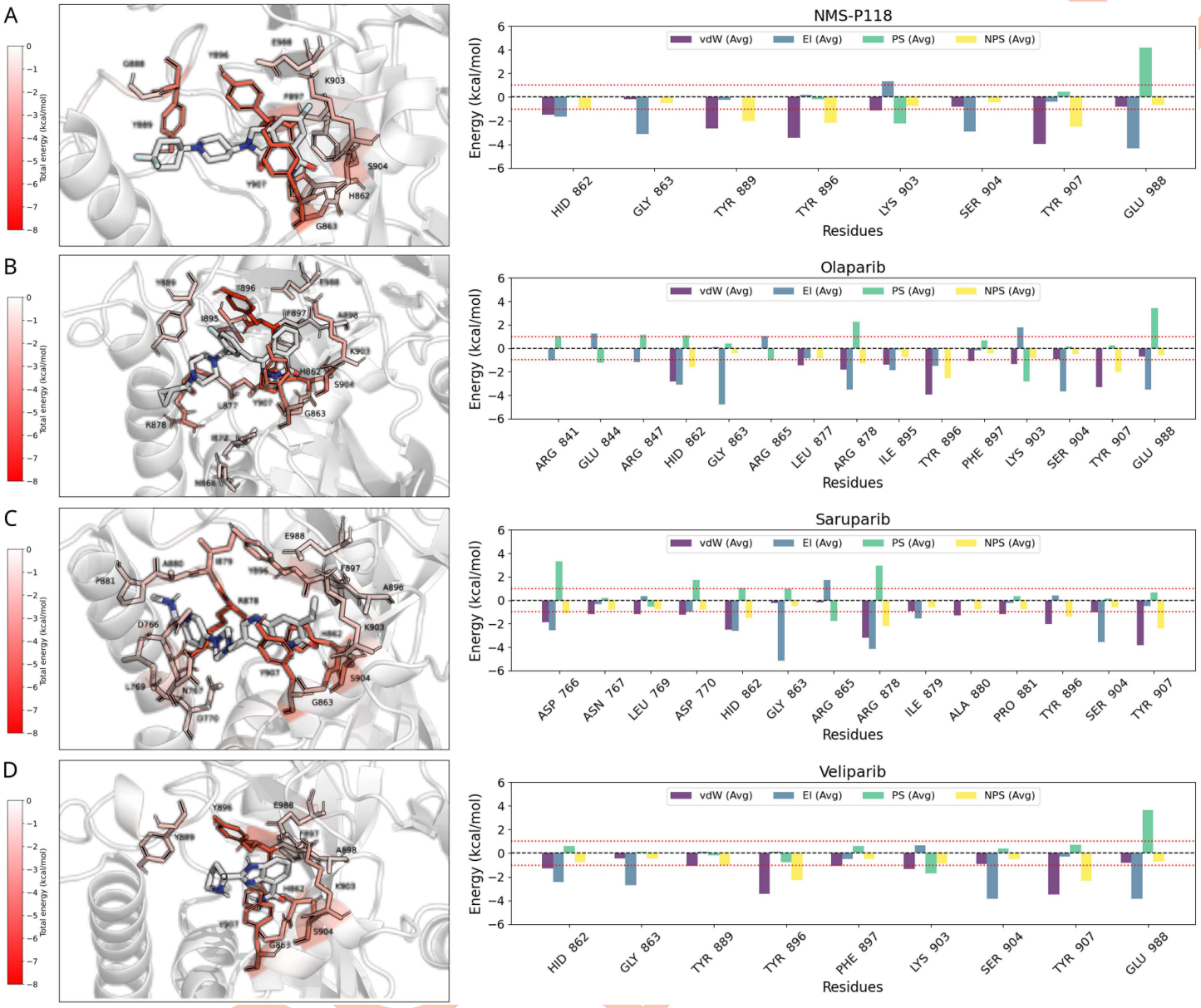

Fig 4. Binding-site energy decomposition for PARP1 in complex with NMS-P118 (A), olaparib (B), saruparib (C), and veliparib (D). The inhibitors are depicted in white while the identified interactions of the residues through a color map. Left panels: per-residue binding free energy decomposition mapped onto the protein surface, colored from low (white) to high (red) energetic contribution (kcal/mol). Right panels: average residue-wise interaction energies between PARP1 and each inhibitor. Only residues with an absolute contribution greater than 1 kcal/mol are displayed (depicted by the dashed red line). Energy components are decomposed into van der Waals (vdW, blue), electrostatic (El, purple), polar solvation (PS, green), and non-polar solvation (NPS, yellow) terms. Negative energy values referred to stabilizing ligand-protein residue contacts while positive values to destabilizing cross-interactions.

https://doi.org/10.1371/journal.pcbi.1014296.g004

2.4 Impact of single-point mutations in PARP1-saruparib binding interaction energy

To gain deeper insight into the residue-level determinants of selective inhibitors of PARP1 such as saruparib, we now apply a systematic mutational analysis targeting key amino acids within the active site, previously identified as major

interactions in the bound-state (Figs 3 and 4). We have selected saruparib for these calculations over NMS-P118 not only due to its larger, experimentally reported selectivity [40], but also because it exhibits several distinctive features: (1) it shows the most pronounced difference in PMF profiles between PARP1 and PARP2 (Fig 1D); (2) it retains a high degree of PARP1 conformational flexibility (see Section V, Fig HC and Fig HH of the S1 Appendix for further details), although this does not fully explain the observed selectivity, it highlights that the binding contacts are more specific and structurally constrained in this complex; and (3) it forms a broad set of intermolecular contacts (Fig 3I), particularly involving its core and tail regions. These features make saruparib the most informative model among the different tested inhibitors to dissect the residue specific contributions of ligand binding. The mutated residues are selected based on contact frequency—specifically those within the active site forming interactions with the largest number of heavy atoms in saruparib. This criterion provides a complementary view of binding determinants, as mutating these residues to glycine is expected to simultaneously disrupt multiple protein–ligand contacts, thereby revealing the extent to which binding stability depends on an intricate network of side-chain interactions. In particular, residues are chosen according to the number of contacts established with saruparib when measured from their C_α atom within a 6 Å cut-off distance, offering an alternative perspective to that presented in Fig 3. By replacing the selected residues with glycine, side-chain contributions are minimized, allowing the assessment of their roles in maintaining the integrity of the ligand-protein binding. The targeted residues—LEU877, ARG878, ILE879, ILE895, and ASN906—were identified as major contributors, among few others, to saruparib PARP1-binding. To systematically evaluate their energetic relevance, different mutation sets are generated, comprising simultaneous replacements of five, three, or two amino acids, thereby enabling a graded assessment of their collective impact on ligand stabilization. Contact maps of the active-site region for the wild-type and mutant complexes (Fig 5A–5D) reveal pronounced alterations in the protein–ligand interaction network. In the wild-type PARP1–saruparib complex (Fig 5A), an extensive network of close, highly frequent contacts is observed, reflecting multiple cooperative stabilizing interactions between the ligand and the surrounding protein residues within the pocket.

Mutation of five key residues to glycine (PARP1–5GLY mutant: LEU877, ARG878, ILE879, ILE895, and ASN906; Fig 5B) leads to a substantial reduction in ligand-protein contacts across the catalytic site, particularly affecting both the 877–879 segment and the 895–906 region. In the triple glycine mutant (PARP1–3GLY: LEU877, ARG878, ILE879; Fig 5C), the loss of contacts within the 877–879 region is retained, while interactions between residues 895–906 are largely preserved. This indicates that the main hotspot for stabilizing interactions is within the 877–879 segment. The double glycine mutant (PARP1–2GLY: ILE895 and ASN906; Fig 5D) exhibits only a moderate reduction in interaction intensity, while the overall contact pattern remains largely comparable to that of the wild-type complex (Fig 5A). The structural visualization of the catalytic site (Fig 5E) highlights the mutated residues in red, illustrating their spatial arrangement within the binding cleft and their contribution to shaping the complementary surface accommodating saruparib. Collectively, these analyses suggest that while the binding interface is broadly distributed across the catalytic pocket, the 877–879 segment represents a major hotspot for stabilizing ligand interactions, whereas other residues primarily modulate interaction strength without markedly altering the overall intermolecular contact landscape and binding pose.

Next, we quantify the variations in the molecular interaction network found across different contact maps through PMF calculations, providing a detailed energetic description of the binding interaction strength for the wild-type *vs.* mutated PARP1 sequences in complex with saruparib. The resulting PMF profiles, depicted in Fig 5F, and their corresponding minimum values in Fig 5G, reveal a systematic modulation of the binding free energy landscape as a function of the number of glycine substitutions. The wild-type PARP1 complex (maroon curve) is characterized by a deep, well-defined global minimum of –17.5 kcal/mol, reflecting a highly stable interaction driven by optimal complementarity between the ligand and the intact active site. The profile displays a smooth descent into the energy well, indicative of a smooth pathway for ligand association.

We find that while the introduction of mutations progressively diminishes the binding stability, the effect is not entirely uniform across the different mutants. The double glycine mutant (PARP1–2GLY; grey curve) exhibits a well-defined

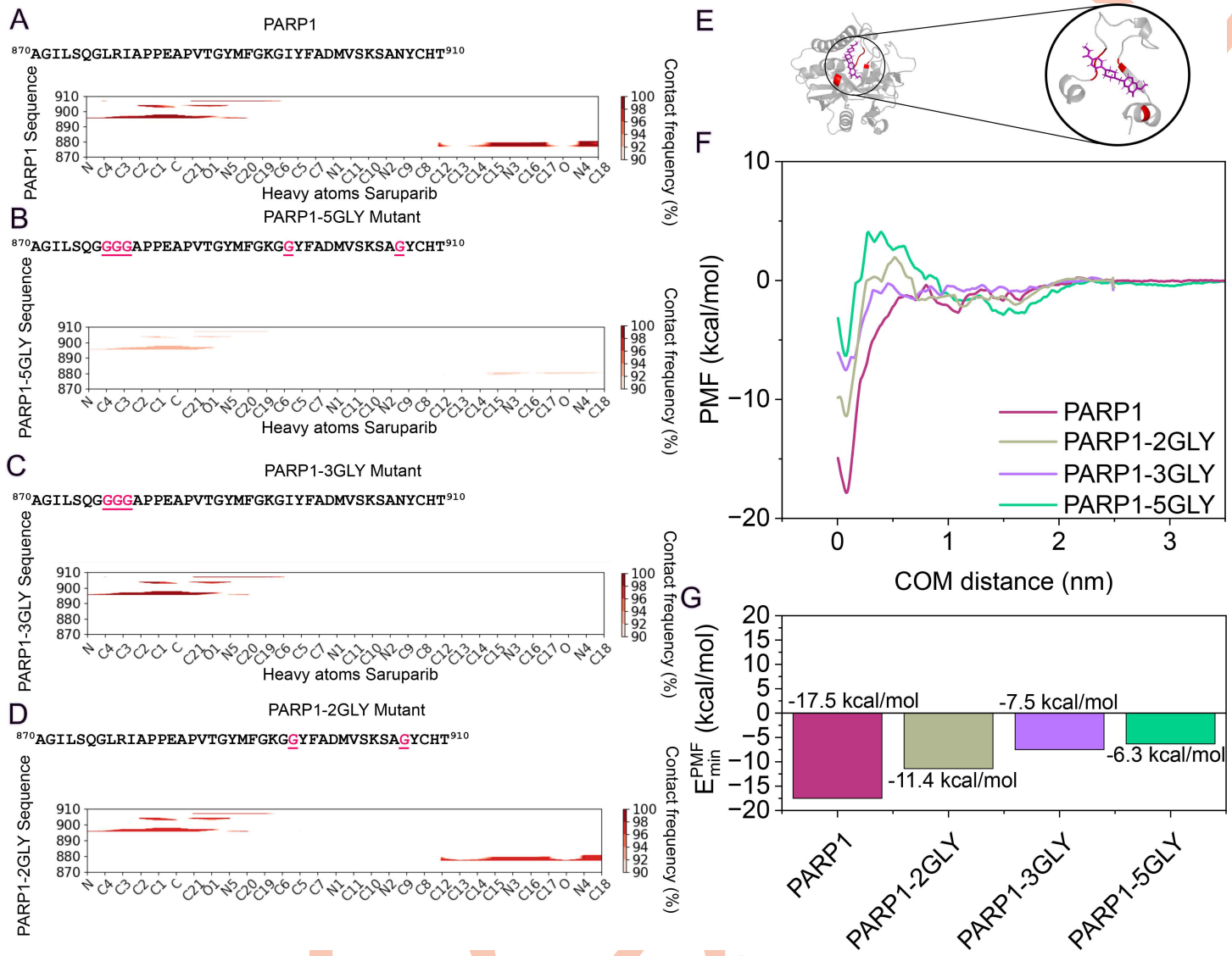

Fig 5. Residue–ligand contact frequency maps for saruparib bound to PARP1 (A) and its glycine-substituted variants: 5GLY (B), 3GLY (C), and 2GLY (D). The PARP1 sequence region corresponding to residues 870–910 is shown above each map, with glycine substitution sites highlighted in red. Contact frequencies are calculated between the heavy atoms of saruparib and the protein residues within the active site. **(E)** Cartoon representation of the PARP1 active site in complex with saruparib highlighting the mutated amino acids in red for the 5GLY mutant. **(F)** PMF profiles for saruparib-PARP1 complex and the glycine mutants (PARP1-2GLY, PARP1-3GLY, and PARP1-5GLY), computed as a function of the center-of-mass distance between the ligand and the protein binding pocket. **(G)** Comparison of the minimum binding free energy values obtained from the PMF curves in **(F)**.

https://doi.org/10.1371/journal.pcbi.1014296.g005

minimum of –11.4 kcal/mol—shallower than the wild-type but still clearly favorable. Nevertheless, the reduction in depth by approximately 6 kcal/mol highlights the importance of these two residues controlling the binding affinity. Notably, the emergence of more pronounced energy barriers at intermediate distances suggests that the mutated residues may also play a role in favoring the ligand pathway into the active site. In contrast, the triple mutant (PARP1–3GLY, violet curve) displays a less stable minimum of –7.5 kcal/mol, reflecting the energetic contributions of the additional side chains to the final bound state. In this case, the dominant effect is not the emergence of intermediate barriers but rather a destabilization of the binding minimum itself, underscoring the significant role of these three residues in maintaining the thermodynamic stability

of the complex. Finally, the most severe energetic perturbation is observed for the quintuple mutant (PARP1–5GLY, green curve), where both effects combine: the minimum rises further to –6.3 kcal/mol, and the PMF profile shows a more pronounced energy barrier of 4.5 kcal/mol preceding it. This indicates that the extensive loss of complementary interactions simultaneously weakens the final bound state and introduces significant hurdles to ligand attachment, likely associated with desolvation penalties triggered by the absence of stabilizing protein contacts.

Collectively, our PMF calculations indicate that the high-affinity binding of saruparib to PARP1 cannot be attributed to a single dominant interaction, but instead emerges from a cooperative network of multiple residue contacts. This conclusion is supported by the observation that mutating a single residue (ARG878) produces only localized changes in the interaction network and results in a modest perturbation of the overall protein–ligand binding free energy (Fig I of the S1 Appendix), although it may be crucial for binding selectivity [54] (see Fig 3I-3J). In contrast, simultaneous mutation of several key residues to glycine leads to cumulative perturbations of the interaction network, resulting in a measurable impact on the thermodynamics of binding. This detailed energetic mapping provides a molecular framework for interpreting structure–activity relationships and offers mechanistic guidance for the rational design of inhibitors with enhanced selectivity. To assess whether this behavior depends on the specific nature of the mutations, we performed the same set of calculations replacing glycine substitutions with alanine mutations. The results show the same overall energetic trend, although the free-energy barriers separating the mutant states are less differentiated in the alanine mutants (Fig L of the S1 Appendix). The PARP2–saruparib system was not considered for the mutational analysis. The calculated binding free energy for this complex is significantly weaker than that observed for PARP1, suggesting that residue-specific perturbations would likely produce only minor energetic differences. For completeness, the full set of contact maps for the mutant complexes is presented in Fig J of the S1 Appendix.

3 Discussion

In this work, we present an atomistic study of how four representative PARP inhibitors engage PARP1 and PARP2, and how these interactions collectively contribute to binding selectivity. By performing atomistic MD simulations and computing contact frequency maps, energy decomposition analyses, umbrella sampling potential-of-mean-force calculations, and targeted mutational perturbations, we demonstrate that selectivity is driven by a cooperative multivalent network of stabilizing contacts anchoring the ligand within the pocket. Such network of intermolecular contacts governs the thermodynamic stability and binding free energy of the ligand-protein complex.

PMF calculations help clarify the mechanistic basis of selectivity (Fig 1). We find that selective inhibitors such as NMS-P118 and saruparib show the largest differences in binding free energy between PARP1 and PARP2, displaying binding landscapes that not only favor the formation of the desired complex but also present energetic barriers hindering association with the non-target paralog, whereas non-selective compounds exhibit smoother energy surfaces that facilitate association with both proteins. In other words, specificity can be partially regulated by the association energy pathway rather than solely in the thermodynamic stability of the end-point. Notably, comparison of PMF-derived ΔG values with experimental estimates obtained from IC_{50} measurements reveals a remarkable correlation, indicating that simulations reproduce the relative selectivity of the inhibitors despite systematic offsets in absolute free energies (Fig 2).

Our contact frequency analysis provide microscopic insights into the binding mechanism in agreement with experimental observations, highlighting the central amino acid–ligand interactions most critical for stable complex formation. The most frequent contacts are notably preserved between PARP1 and PARP2, and are primarily mediated by a tyrosine triad through van der Waals interactions (TYR889, TYR896, TYR907 in PARP1; TYR455, TYR462, TYR473 in PARP2). Contact frequency and energetic decomposition analyses reveal a conserved network of stabilizing interactions that defines the bound-state pose within the catalytic pocket. These common interactions are necessary for binding to the active site, while selectivity arises from how these contacts are energetically weighted, and how other contributing interactions—mostly electrostatic—cooperatively emerge to define the protein-ligand binding free energy (Figs 3, 4).

The mechanistic picture given by the molecular contact analysis and the thermodynamic evaluation provided by PMF calculations with increasing number of residue mutations have direct implications in binding affinity. Maximizing selectivity requires more than lowering the overall binding free energy, instead relying on design choices that enhance interactions with structural features surrounding the binding pocket, stabilize the desired bound conformation, and suppress off-target binding. In that sense, identifying the key contacts driving ligand-complex stabilization—and how these contacts cooperatively reshape the binding association pathway—is fundamental to maximizing specific binding. Our mutational perturbation analysis demonstrates that selective binding relies on multivalent cooperative interactions, rather than on single dominant interaction modes (Fig 5). Specifically, simultaneous mutation of five key amino acids to glycine within the binding interface reduces binding affinity by more than 50%, thereby preventing stable complex formation. Therefore, designing ligands that engage multiple complementary motifs—e.g., multivalent—likely yields more durable protein-specific inhibitors than ligands relying on a highly specific binding mode.

Taken together, our study highlights PARP inhibitor selectivity as an energy landscape problem: the critical question is not simply how tightly a ligand binds, but how the entire route to binding is shaped and modulated by a cooperative network of ligand–protein interactions. Future studies could also explore the role of regulatory partners such as HPF1, which can reshape the active site and modulate the electrostatic and hydrogen-bonding environment, potentially influencing inhibitor binding and selectivity. By computing contact molecular networks and potential-of-mean-force calculations, we propose a computational framework to guide and rationalize the design of next-generation enzyme-selective inhibitors with improved efficacy and safety.

Materials and methods

3.1 Atomistic system preparation and force field

All protein-ligand complexes were prepared using the GROMACS 2023 package in explicit water at 150 mM NaCl. Proteins were modeled using the a99SB-disp force field, which accurately reproduces protein conformational ensembles, while ligands were parameterized with the OpenFF force field. Systems were solvated in cubic boxes with periodic boundary conditions, neutralized, and energy-minimized. Bond constraints for hydrogen-containing bonds were applied using LINCS, enabling a 2 fs timestep. Temperature and pressure were controlled with the v-rescale thermostat and Parrinello–Rahman barostat.

3.2 Potential of Mean Force (PMF) calculations

PMFs were computed to quantify the unbinding free energies of ligands from their target proteins by describing how the interaction energy changes as a function of their separation along a chosen reaction coordinate.

First, all systems were prepared and equilibrated in explicit solvent at 150 mM NaCl using the a99SB-disp force field for proteins and OpenFF for ligands, ensuring an accurate description of protein–ligand and solvent interactions. Next, ligand dissociation was defined along a center-of-mass (COM) distance reaction coordinate between the ligand and the protein binding site. This coordinate was selected because it follows the path with the least steric hindrance in the tri-dimensional structure and is consistently applicable across all systems (see Fig M in S1 Appendix for a depiction of the chosen reaction coordinate).

To sample the dissociation process, approximately 60 umbrella sampling windows were generated along the reaction coordinate, each separated by 0.5 Å. Each window was subjected to energy minimization (force tolerance 1000 kJ mol^{-1} nm^{-1}), followed by a short 1 ns NpT equilibration with positional restraints of 10000 kJ mol^{-1} nm^{-2} applied to the heavy atoms of both the protein and the ligand. Production simulations were then performed for each window.

Subsequently, the free energy profiles were reconstructed using the Weighted Histogram Analysis Method (WHAM), discarding the initial 10% of each trajectory as equilibration. From the resulting PMF profiles, we identify the energetic

minimum corresponding to the bound state and estimate the free energy barriers associated with ligand dissociation. Finally, statistical uncertainties were estimated via block averaging over trajectory segments, and convergence was assessed by comparing PMFs obtained from cumulative simulation times (2–4 ns, 2–6 ns, 2–8 ns, and 2–10 ns), as shown in Fig K in S1 Appendix.

3.3 Contact map analysis

Intermolecular and intramolecular contact maps were derived from MD trajectories. Contacts were defined using a sequence-dependent cutoff distance based on the excluded volume of each residue, whereas ligand heavy atoms were assigned a fixed cutoff of 6 Å. In particular, protein–ligand contacts were computed between the heavy atoms of the ligand and the center of mass of the side chains of the amino acids. Contact frequencies are reported as percentages over the trajectory, providing insight into the most persistent interactions.

3.4 Binding Free Energy and Hydrogen Bond Analysis

Ligand binding energies were estimated using the MM-GBSA approach (AmberTools23), decomposed per residue to identify key contributors. Electrostatic, van der Waals, polar, and nonpolar solvation contributions were computed. Hydrogen bonds were identified geometrically (donor-acceptor distance <3.0 Å, angle >135°) and occupancies above 50% were reported.

For full simulation details see S1 Appendix. We provide the relevant data in the repository (GitHub link for the repository) to facilitate reproducibility of our results. In the repository we also give the necessary code to run the simulations and accessible instructions to obtain our results.

Supporting information

S1 Appendix. Fig A Atomistic PMF dissociation profiles for ligand–PARP complexes. Potential of mean force (PMF) profiles describing the dissociation between each ligand and PARP1/PARP2 under physiological NaCl concentration (150 mM) and room conditions, in explicit solvent and ions. The center-of-mass (COM) distance between the protein binding pocket and the ligand is used as the reaction coordinate. Curves are shown for saruparib (A) and veliparib (B). The statistical uncertainty is represented as color shadowing corresponding to the standard deviation obtained from trajectory segments. **Fig B Comparison between experimental and simulated binding free energy differences.** Experimental $(\Delta(\Delta G_{\text{Experimental}})_{\text{PARP1–PARP2}})$ and simulated $(\Delta(\Delta G_{\text{PMF Simulation}})_{\text{PARP1–PARP2}})$ binding free energy differences for different inhibitors (saruparib, NMS-P118, veliparib, and olaparib). A linear shading is included as a guide to the eye. PARP1-selective inhibitors are represented as stars, whereas non-selective inhibitors are shown as circles. **Fig C Intermolecular contact frequency maps for PARP1 and PARP2.** Contact frequency maps between protein residues and ligand heavy atoms. Panels (A–D) correspond to PARP1 in complex with NMS-P118, saruparib, olaparib, and veliparib, respectively. Panels (E–H) correspond to the same ligands in complex with PARP2. Contacts are represented as percentage frequencies. **Fig D Binding site interaction energies for PARP2–ligand complexes.** Per-residue binding free energy decomposition mapped onto the protein surface for NMS-P118 (A), olaparib (B), saruparib (C), and veliparib (D). Left panels show total contributions, while right panels display the decomposition into van der Waals, electrostatic, polar solvation, and non-polar solvation components. Only residues with contributions larger than 1 kcal/mol are shown. **Fig E MM-GBSA binding free energy profiles for PARP1 complexes.** (A) Binding free energy profiles along molecular dynamics trajectories for different inhibitors. (B–E) Per-residue energy decomposition for NMS-P118, olaparib, saruparib, and velipa-rib, respectively. The red dashed line indicates the threshold used to identify significant contributions. **Fig F MM-GBSA binding free energy profiles for PARP2 complexes.** (A) Binding free energy profiles along molecular dynamics trajectories for different inhibitors. (B–E) Per-residue energy decomposition for NMS-P118, olaparib, saruparib, and veliparib,

respectively. The red dashed line indicates the threshold used to identify significant contributions. **Fig G Hydrogen bond analysis for PARP–ligand complexes.** Summary of hydrogen bonds detected between PARP1 or PARP2 and different inhibitors (NMS-P118, olaparib, saruparib, and veliparib) in molecular dynamics simulations. Only interactions with occupancy above 50% are reported. **Fig H Structural dynamics of PARP1 and PARP2.** RMSF and RMSD analyses for PARP1 and PARP2 in apo form and in complex with different inhibitors. Flexible regions and ligand-induced stabilization effects are highlighted using per-residue RMSF mapping onto protein structures. **Fig I Effect of glycine mutation on ligand binding.** Residue–ligand contact frequency maps between saruparib and PARP1 (A) and the 1GLY mutant (B). (C) PMF profiles for ligand unbinding from both systems, including extracted binding free energy minima. **Fig J Contact frequency maps for multiple glycine mutants.** Residue–ligand contact maps between saruparib and different glycine mutants (1GLY, 2GLY, 3GLY, and 5GLY), highlighting the progressive disruption of intermolecular interactions. **Fig K PMF convergence analysis.** Convergence of the PMF profile for the PARP1–saruparib complex using cumulative trajectory segments of increasing length (2–4 ns, 2–6 ns, 2–8 ns, and 2–10 ns). **Fig L PMF profiles for alanine mutants.** PMF profiles for saruparib unbinding from PARP1 and alanine mutants (2ALA, 3ALA, and 5ALA), computed along the center-of-mass distance between ligand and binding pocket. **Fig M Reaction coordinate for PMF calculations.** Three orthogonal views of the protein–ligand complex showing the chosen reaction coordinate for PMF calculations. The arrows indicate the center-of-mass (COM) distance along which the ligand (veliparib) unbinding was sampled. **Fig N Comparison of the PMF profiles for the PARP1–saruparib complex calculated using different dimensional descriptions.**
(PDF)

Acknowledgments

This work has also been performed using resources provided by Archer2 (https://www.archer2.ac.uk/) funded by EPSRC Tier-2 capital grant EP/P020259/e829. The authors also thankfully acknowledge RES computational resources provided by Mare Nostrum 5 through the activities 2024-3- 0001 and 2025-1-0009.

Author contributions

Conceptualization: Alejandro Feito, Adiran Garaizar, Alberto Ocana, Jorge R. Espinosa.

Data curation: Alejandro Feito, Natàlia DeMoya-Valenzuela, Cristian Privat, Andrés R. Tejedor.

Formal analysis: Alejandro Feito, Natàlia DeMoya-Valenzuela, Cristian Privat.

Funding acquisition: Alberto Ocana, Jorge R. Espinosa.

Investigation: Alejandro Feito, Lucía Paniagua-Herranz, Adiran Garaizar, Alberto Ocana, Jorge R. Espinosa.

Methodology: Alejandro Feito, Natàlia DeMoya-Valenzuela, Cristian Privat, Andrés R. Tejedor.

Project administration: Alberto Ocana, Jorge R. Espinosa.

Resources: Alberto Ocana, Jorge R. Espinosa.

Software: Alejandro Feito, Natàlia DeMoya-Valenzuela, Cristian Privat, Andrés R. Tejedor.

Supervision: Andrés R. Tejedor, Alberto Ocana, Jorge R. Espinosa.

Validation: Adiran Garaizar.

Visualization: Alejandro Feito, Natàlia DeMoya-Valenzuela, Cristian Privat, Jorge R. Espinosa.

Writing – original draft: Alejandro Feito, Natàlia DeMoya-Valenzuela, Cristian Privat, Andrés R. Tejedor, Lucía Paniagua-Herranz, Adiran Garaizar, Alberto Ocana, Jorge R. Espinosa.

Writing – review & editing: Alejandro Feito, Natàlia DeMoya-Valenzuela, Cristian Privat, Andrés R. Tejedor, Lucía Paniagua-Herranz, Adiran Garaizar, Alberto Ocana, Jorge R. Espinosa.

References

1. Ko HL, Ren EC. Functional sspects of PARP1 in DNA repair and transcription. Biomolecules. 2012;2(4):524–48. https://doi.org/10.3390/biom2040524 PMID: 24970148
2. Ray Chaudhuri A, Nussenzweig A. The multifaceted roles of PARP1 in DNA repair and chromatin remodelling. Nat Rev Mol Cell Biol. 2017;18(10):610–21. https://doi.org/10.1038/nrm.2017.53 PMID: 28676700
3. Eustermann S, Wu W-F, Langelier M-F, Yang J-C, Easton LE, Riccio AA, et al. Structural basis of detection and signaling of DNA single-strand breaks by human PARP-1. Mol Cell. 2015;60(5):742–54. https://doi.org/10.1016/j.molcel.2015.10.032 PMID: 26626479
4. Ronson GE, Piberger AL, Higgs MR, Olsen AL, Stewart GS, McHugh PJ, et al. PARP1 and PARP2 stabilise replication forks at base excision repair intermediates through Fbh1-dependent Rad51 regulation. Nat Commun. 2018;9(1):746. https://doi.org/10.1038/s41467-018-03159-2 PMID: 29467415
5. Sinha S, Molla S, Kundu CN. PARP1-modulated chromatin remodeling is a new target for cancer treatment. Med Oncol. 2021;38(10):118. https://doi.org/10.1007/s12032-021-01570-2 PMID: 34432161
6. Zong W, Gong Y, Sun W, Li T, Wang Z-Q. PARP1: liaison of chromatin remodeling and transcription. Cancers (Basel). 2022;14(17):4162. https://doi.org/10.3390/cancers14174162 PMID: 36077699
7. Alemasova EE, Lavrik OI. A sePARate phase? Poly(ADP-ribose) versus RNA in the organization of biomolecular condensates. Nucleic Acids Res. 2022;50(19):10817–38. https://doi.org/10.1093/nar/gkac866 PMID: 36243979
8. Ho Y-C, Ku C-S, Tsai S-S, Shiu J-L, Jiang Y-Z, Miriam HE, et al. PARP1 recruits DNA translocases to restrain DNA replication and facilitate DNA repair. PLoS Genet. 2022;18(12):e1010545. https://doi.org/10.1371/journal.pgen.1010545 PMID: 36512630
9. Lu Y, Fu W, Xing W, Wu H, Zhang C, Xu D. Transcriptional regulation mechanism of PARP1 and its application in disease treatment. Epigenetics Chromatin. 2024;17(1):26. https://doi.org/10.1186/s13072-024-00550-w PMID: 39118189
10. Gong Y, Wang Z, Zong W, Shi R, Sun W, Wang S, et al. PARP1 UFMylation ensures the stability of stalled replication forks. Proc Natl Acad Sci U S A. 2024;121(18):e2322520121. https://doi.org/10.1073/pnas.2322520121 PMID: 38657044
11. Módis K, Gero D, Erdélyi K, Szoleczky P, DeWitt D, Szabo C. Cellular bioenergetics is regulated by PARP1 under resting conditions and during oxidative stress. Biochem Pharmacol. 2012;83(5):633–43. https://doi.org/10.1016/j.bcp.2011.12.014 PMID: 22198485
12. Faraoni I, Graziani G. Role of BRCA mutations in cancer treatment with Poly(ADP-ribose) Polymerase (PARP) inhibitors. Cancers (Basel). 2018;10(12):487. https://doi.org/10.3390/cancers10120487 PMID: 30518089
13. Dilmac S, Ozpolat B. Mechanisms of PARP-inhibitor-resistance in BRCA-mutated breast cancer and new therapeutic approaches. Cancers (Basel). 2023;15(14):3642. https://doi.org/10.3390/cancers15143642 PMID: 37509303
14. Boussios S, Karihtala P, Moschetta M, Abson C, Karathanasi A, Zakynthinakis-Kyriakou N, et al. Veliparib in ovarian cancer: a new synthetically lethal therapeutic approach. Invest New Drugs. 2019;38(1):181–93. https://doi.org/10.1007/s10637-019-00867-4
15. Cortesi L, Rugo HS, Jackisch C. An overview of PARP inhibitors for the treatment of breast cancer. Target Oncol. 2021;16(3):255–82. https://doi.org/10.1007/s11523-021-00796-4 PMID: 33710534
16. Zeng Y, Arisa O, Peer C, Figg W, Fojo A. PARP inhibitors: a review of the pharmacology, pharmacokinetics, and pharmacogenetics. Seminars in Oncology. 2023. https://doi.org/10.1053/j.seminoncol.2023.09.005
17. Jain PG, Patel BD. Medicinal chemistry approaches of poly ADP-Ribose polymerase 1 (PARP1) inhibitors as anticancer agents - A recent update. Eur J Med Chem. 2019;165:198–215. https://doi.org/10.1016/j.ejmech.2019.01.024 PMID: 30684797
18. Herencia-Ropero A, Llop-Guevara A, Staniszewska AD, Domènech-Vivó J, García-Galea E, Moles-Fernández A, et al. The PARP1 selective inhibitor saruparib (AZD5305) elicits potent and durable antitumor activity in patient-derived BRCA1/2-associated cancer models. Genome Med. 2024;16(1):107. https://doi.org/10.1186/s13073-024-01370-z PMID: 39187844
19. Yoshida K, Miki Y. Role of BRCA1 and BRCA2 as regulators of DNA repair, transcription, and cell cycle in response to DNA damage. Cancer Sci. 2004;95(11):866–71. https://doi.org/10.1111/j.1349-7006.2004.tb02195.x PMID: 15546503
20. Tarsounas M, Sung P. The antitumorigenic roles of BRCA1-BARD1 in DNA repair and replication. Nat Rev Mol Cell Biol. 2020;21(5):284–99. https://doi.org/10.1038/s41580-020-0218-z PMID: 32094664
21. Chan CY, Tan KV, Cornelissen B. PARP inhibitors in cancer diagnosis and therapy. Clin Cancer Res. 2021;27(6):1585–94. https://doi.org/10.1158/1078-0432.CCR-20-2766 PMID: 33082213
22. Bhamidipati D, Haro-Silerio JI, Yap TA, Ngoi N. PARP inhibitors: enhancing efficacy through rational combinations. Br J Cancer. 2023;129(6):904–16. https://doi.org/10.1038/s41416-023-02326-7 PMID: 37430137
23. Rudolph J, Jung K, Luger K. Inhibitors of PARP: number crunching and structure gazing. Proc Natl Acad Sci U S A. 2022;119(11):e2121979119. https://doi.org/10.1073/pnas.2121979119 PMID: 35259019
24. Rimar KJ, Tran PT, Matulewicz RS, Hussain M, Meeks JJ. The emerging role of homologous recombination repair and PARP inhibitors in genitourinary malignancies. Cancer. 2017;123(11):1912–24. https://doi.org/10.1002/cncr.30631 PMID: 28323334
25. Pálinkás HL, Pongor L, Balajti M, Nagy Á, Nagy K, Békési A, et al. Primary founder mutations in the PRKDC gene increase tumor mutation load in colorectal cancer. Int J Mol Sci. 2022;23(2):633. https://doi.org/10.3390/ijms23020633 PMID: 35054819

26. Ryan K, Bolaños B, Smith M, Palde PB, Cuenca PD, VanArsdale TL, et al. Dissecting the molecular determinants of clinical PARP1 inhibitor selectivity for tankyrase1. J Biol Chem. 2021;296:100251. https://doi.org/10.1074/jbc.RA120.016573 PMID: 33361107
27. Gunderson CC, Moore KN. Olaparib: an oral PARP-1 and PARP-2 inhibitor with promising activity in ovarian cancer. Future Oncol. 2015;11(5):747–57. https://doi.org/10.2217/fon.14.313 PMID: 25757679
28. Murai J, Huang SN, Das BB, Renaud A, Zhang Y, Doroshow JH, et al. Trapping of PARP1 and PARP2 by clinical PARP inhibitors. Cancer Res. 2012;72(21):5588–99. https://doi.org/10.1158/0008-5472.CAN-12-2753 PMID: 23118055
29. Robillard L, Nguyen M, Harding TC, Simmons AD. Abstract 2475: in vitro and in vivo assessment of the mechanism of action of the PARP inhibitor rucaparib. Cancer Research. 2017;77(13_Supplement):2475–2475. https://doi.org/10.1158/1538-7445.am2017-2475
30. Musella A, Bardhi E, Marchetti C, Vertechy L, Santangelo G, Sassu C, et al. Rucaparib: an emerging parp inhibitor for treatment of recurrent ovarian cancer. Cancer Treat Rev. 2018;66:7–14. https://doi.org/10.1016/j.ctrv.2018.03.004 PMID: 29605737
31. Mirza MR, Monk BJ, Herrstedt J, Oza AM, Mahner S, Redondo A, et al. Niraparib maintenance therapy in platinum-sensitive, recurrent ovarian cancer. N Engl J Med. 2016;375(22):2154–64. https://doi.org/10.1056/NEJMoa1611310 PMID: 27717299
32. González-Martín A, Pothuri B, Vergote I, DePont Christensen R, Graybill W, Mirza MR, et al. Niraparib in patients with newly diagnosed advanced ovarian cancer. N Engl J Med. 2019;381(25):2391–402. https://doi.org/10.1056/NEJMoa1910962 PMID: 31562799
33. Litton JK, Rugo HS, Ettl J, Hurvitz SA, Gonçalves A, Lee K-H, et al. Talazoparib in Patients with Advanced Breast Cancer and a Germline BRCA Mutation. N Engl J Med. 2018;379(8):753–63. https://doi.org/10.1056/NEJMoa1802905 PMID: 30110579
34. Agarwal N, Azad AA, Carles J, Fay AP, Matsubara N, Heinrich D, et al. Talazoparib plus enzalutamide in men with first-line metastatic castration-resistant prostate cancer (TALAPRO-2): a randomised, placebo-controlled, phase 3 trial. Lancet. 2023;402(10398):291–303. https://doi.org/10.1016/S0140-6736(23)01055-3 PMID: 37285865
35. Shen Y, Aoyagi-Scharber M, Wang B. Trapping Poly(ADP-Ribose) Polymerase. J Pharmacol Exp Therap. 2015;353:446–57. https://doi.org/10.1124/jpet.114.222448
36. Johannes JW, Balazs AY, Barratt D, Bista M, Chuba MD, Cosulich S. Discovery of 6-Fluoro-5-{4-[(5-fluoro-2-methyl-3-oxo-3, 4-dihydroquinoxalin-6-yl) methyl] piperazin-1-yl}-N-methylpyridine-2-carboxamide (AZD9574): a CNS-Penetrant, PARP1-Selective Inhibitor. J Med Chem. 2024;67(24):21717–28.
37. Papeo G, Posteri H, Borghi D, Busel AA, Caprera F, Casale E. Discovery of 2-[1-(4, 4-difluorocyclohexyl) piperidin-4-yl]-6-fluoro-3-oxo-2, 3-dihydro-1 H-isoindole-4-carboxamide (NMS-P118): a potent, orally available, and highly selective parp-1 inhibitor for cancer therapy. J Med Chem. 2015;58(17):6875–98.
38. LaFargue CJ, Dal Molin GZ, Sood AK, Coleman RL. Exploring and comparing adverse events between PARP inhibitors. Lancet Oncol. 2019;20(1):e15–28. https://doi.org/10.1016/S1470-2045(18)30786-1 PMID: 30614472
39. Zheng J, Li Z, Min W. Current status and future promise of next-generation poly (ADP-Ribose) polymerase 1-selective inhibitor AZD5305. Front Pharmacol. 2023;13:979873. https://doi.org/10.3389/fphar.2022.979873 PMID: 36756144
40. Illuzzi G, Staniszewska AD, Gill SJ, Pike A, McWilliams L, Critchlow SE, et al. Preclinical Characterization of AZD5305, A Next-Generation, Highly Selective PARP1 Inhibitor and Trapper. Clin Cancer Res. 2022;28(21):4724–36. https://doi.org/10.1158/1078-0432.CCR-22-0301 PMID: 35929986
41. Azad A, Agarwal N, Armstrong AJ, Hellmis E, Schlürmann F, Sugimoto M, et al. Phase III, double-blind, placebo-controlled, 2-cohort, randomized study of saruparib (AZD5305) in combination with androgen receptor pathway inhibitors in patients with metastatic hormone-sensitive prostate cancer with and without homologous recombination repair mutation (EvoPAR-Prostate01). Am Soc Clin Oncol. 2025.
42. Gibbs-Seymour I, Fontana P, Rack JGM, Ahel I. HPF1/C4orf27 Is a PARP-1-interacting protein that regulates PARP-1 ADP-ribosylation activity. Mol Cell. 2016;62(3):432–42. https://doi.org/10.1016/j.molcel.2016.03.008 PMID: 27067600
43. Kurgina TA, Moor NA, Kutuzov MM, Naumenko KN, Ukraintsev AA, Lavrik OI. Dual function of HPF1 in the modulation of PARP1 and PARP2 activities. Commun Biol. 2021;4(1):1259. https://doi.org/10.1038/s42003-021-02780-0 PMID: 34732825
44. Rudolph J, Roberts G, Luger K. Histone parylation factor 1 contributes to the inhibition of PARP1 by cancer drugs. Nat Commun. 2021;12(1):736. https://doi.org/10.1038/s41467-021-20998-8 PMID: 33531508
45. Thorsell A-G, Ekblad T, Karlberg T, Löw M, Pinto AF, Trésaugues L, et al. Structural basis for potency and promiscuity in Poly(ADP-ribose) Polymerase (PARP) and Tankyrase inhibitors. J Med Chem. 2017;60(4):1262–71. https://doi.org/10.1021/acs.jmedchem.6b00990 PMID: 28001384
46. Bondar D, Karpichev Y. Poly(ADP-Ribose) Polymerase (PARP) inhibitors for cancer therapy: advances, challenges, and future directions. Biomolecules. 2024;14(10):1269. https://doi.org/10.3390/biom14101269 PMID: 39456202
47. Limongelli V, Marinelli L, Cosconati S, La Motta C, Sartini S, Mugnaini L, et al. Sampling protein motion and solvent effect during ligand binding. Proc Natl Acad Sci U S A. 2012;109(5):1467–72. https://doi.org/10.1073/pnas.1112181108 PMID: 22238423
48. Ross GA, Morris GM, Biggin PC. One Size Does Not Fit All: The Limits of Structure-Based Models in Drug Discovery. J Chem Theory Comput. 2013;9(9):4266–74. https://doi.org/10.1021/ct4004228 PMID: 24124403
49. Aldakheel FM, Alduraywish SA, Dabwan KH. Integrating machine learning driven virtual screening and molecular dynamics simulations to identify potential inhibitors targeting PARP1 against prostate cancer. Sci Rep. 2025;15(1):12764. https://doi.org/10.1038/s41598-025-97208-8 PMID: 40229418

50. Khalid M, H Alqarni M, Foudah AI, Saad Al Oraby M. Reinventing PARP1 inhibition: harnessing virtual screening and molecular dynamics simulations to identify repurposed drugs for anticancer therapeutics. J Biomol Struct Dyn. 2025;43(13):7063–74. https://doi.org/10.1080/07391102.2025.2483963 PMID: 40135853
51. Zhao J, Yu N, Zhao X, Quan W, Shu M. 3D-QSAR, molecular docking, and molecular dynamics analysis of dihydrodiazaindolone derivatives as PARP-1 inhibitors. J Mol Model. 2023;29(5):131. https://doi.org/10.1007/s00894-023-05525-4 PMID: 37020092
52. Hu H, Chen B, Zheng D, Huang G. Revealing the selective mechanisms of inhibitors to PARP-1 and PARP-2 via multiple computational methods. PeerJ. 2020;8:e9241. https://doi.org/10.7717/peerj.9241 PMID: 32509471
53. Nozal V, Beyens O, Peeters S, Fabisiak A, Augustyns K, De Meester I, et al. Highly potent dipeptidyl peptidase 8/9 (DPP8/9) inhibitors designed via relative binding free energy calculations. Eur J Med Chem. 2025;297:117913. https://doi.org/10.1016/j.ejmech.2025.117913 PMID: 40609224
54. Feito S r A, DeMoya-Valenzuela N, Privat C, Tejedor AR, DelValle-Carrillo M, Cembellín S. Benchmarking free energy computational methods for revealing the interactions driving PARP1 selective inhibition. bioRxiv. 2025;2025:2025–12.
55. Karlberg T, Hammarström M, Schütz P, Svensson L, Schüler H. Crystal structure of the catalytic domain of human PARP2 in complex with PARP inhibitor ABT-888. Biochemistry. 2010;49(6):1056–8. https://doi.org/10.1021/bi902079y PMID: 20092359
56. Garaizar A, Espinosa JR, Joseph JA, Collepardo-Guevara R. Kinetic interplay between droplet maturation and coalescence modulates shape of aged protein condensates. Sci Rep. 2022;12(1):4390. https://doi.org/10.1038/s41598-022-08130-2 PMID: 35293386
57. Blazquez S, Sanchez-Burgos I, Ramirez J, Higginbotham T, Conde MM, Collepardo-Guevara R, et al. Location and concentration of aromatic-rich segments dictates the percolating inter-molecular network and viscoelastic properties of ageing condensates. Adv Sci (Weinh). 2023;10(25):e2207742. https://doi.org/10.1002/advs.202207742 PMID: 37386790
58. Tejedor AR, Sanchez-Burgos I, Estevez-Espinosa M, Garaizar A, Collepardo-Guevara R, Ramirez J, et al. Protein structural transitions critically transform the network connectivity and viscoelasticity of RNA-binding protein condensates but RNA can prevent it. Nat Commun. 2022;13(1):5717. https://doi.org/10.1038/s41467-022-32874-0 PMID: 36175408
59. R Tejedor A, Aguirre Gonzalez A, Maristany MJ, Chew PY, Russell K, Ramirez J, et al. Chemically informed coarse-graining of electrostatic forces in charge-rich biomolecular condensates. ACS Cent Sci. 2025;11(2):302–21. https://doi.org/10.1021/acscentsci.4c01617 PMID: 40028356
60. Robustelli P, Piana S, Shaw DE. Developing a molecular dynamics force field for both folded and disordered protein states. Proc Natl Acad Sci U S A. 2018;115(21):E4758–66. https://doi.org/10.1073/pnas.1800690115 PMID: 29735687
61. Aduriz-Arrizabalaga J, Lopez X, De Sancho D. Atomistic molecular simulations of Aβ-Zn conformational ensembles. Proteins. 2024;92(1):134–44. https://doi.org/10.1002/prot.26590 PMID: 37746887
62. Wagner J, Thompson M, Mobley DL, Chodera J, Bannan C, Rizzi A. Openforcefield/openff-toolkit: 0.16.9 minor release. Zenodo. 2025. https://doi.org/10.5281/zenodo.15306573
63. Thomsen R, Christensen MH. MolDock: a new technique for high-accuracy molecular docking. J Med Chem. 2006;49(11):3315–21. https://doi.org/10.1021/jm051197e PMID: 16722650
64. Petropoulos M, Karamichali A, Rossetti GG, Freudenmann A, Iacovino LG, Dionellis VS, et al. Transcription-replication conflicts underlie sensitivity to PARP inhibitors. Nature. 2024;628(8007):433–41. https://doi.org/10.1038/s41586-024-07217-2 PMID: 38509368
65. Menear KA, Adcock C, Boulter R, Cockcroft X, Copsey L, Cranston A, et al. 4-[3-(4-cyclopropanecarbonylpiperazine-1-carbonyl)-4-fluorobenzyl]-2H-phthalazin-1-one: a novel bioavailable inhibitor of poly(ADP-ribose) polymerase-1. J Med Chem. 2008;51(20):6581–91. https://doi.org/10.1021/jm8001263 PMID: 18800822
66. Murai J, Zhang Y, Morris J, Ji J, Takeda S, Doroshow JH, et al. Rationale for poly(ADP-ribose) polymerase (PARP) inhibitors in combination therapy with camptothecins or temozolomide based on PARP trapping versus catalytic inhibition. J Pharmacol Exp Ther. 2014;349(3):408–16. https://doi.org/10.1124/jpet.113.210146 PMID: 24650937
67. Johannes JW, Balazs A, Barratt D, Bista M, Chuba MD, Cosulich S. Discovery of 5-{4-[(7-ethyl-6-oxo-5, 6-dihydro-1, 5-naphthyridin-3-yl) methyl] piperazin-1-yl}-N-methylpyridine-2-carboxamide (AZD5305): a PARP1–DNA trapper with high selectivity for PARP1 over PARP2 and other PARPs. Journal of Medicinal Chemistry. 2021;64(19):14498–512.
68. Kim G, Ison G, McKee AE, Zhang H, Tang S, Gwise T, et al. FDA approval summary: olaparib monotherapy in patients with deleterious germline BRCA-mutated advanced ovarian cancer treated with three or more lines of chemotherapy. Clin Cancer Res. 2015;21(19):4257–61. https://doi.org/10.1158/1078-0432.CCR-15-0887 PMID: 26187614
69. Penning TD, Zhu GD, Gandhi VB, Gong J, Liu X, Shi Y. Discovery of the poly (ADP-ribose) polymerase (PARP) inhibitor 2-[(R)-2-methylpyrrolidin-2-yl]-1 H-benzimidazole-4-carboxamide (ABT-888) for the treatment of cancer. J Med Chem. 2009;52(2):514–23.
70. Huang S-MA, Mishina YM, Liu S, Cheung A, Stegmeier F, Michaud GA, et al. Tankyrase inhibition stabilizes axin and antagonizes Wnt signalling. Nature. 2009;461(7264):614–20. https://doi.org/10.1038/nature08356 PMID: 19759537
71. Steffen JD, Brody JR, Armen RS, Pascal JM. Structural implications for selective targeting of PARPs. Front Oncol. 2013;3:301. https://doi.org/10.3389/fonc.2013.00301 PMID: 24392349
72. Holderbach S, Adam L, Jayaram B, Wade RC, Mukherjee G. RASPD+: fast protein-ligand binding free energy prediction using simplified physicochemical features. Front Mol Biosci. 2020;7:601065. https://doi.org/10.3389/fmolb.2020.601065 PMID: 33392260

73. Rubiales-Martínez A, Martínez J, Mera-Jiménez E, Pérez-Flores J, Téllez-Isaías G, Miranda Ruvalcaba R, et al. Design of two new sulfur derivatives of perezone: in silico study simulation targeting PARP-1 and in vitro study validation using cancer cell lines. Int J Mol Sci. 2024;25(2):868. https://doi.org/10.3390/ijms25020868 PMID: 38255943

74. Garaizar A, Espinosa JR, Joseph JA, Krainer G, Shen Y, Knowles TPJ, et al. Aging can transform single-component protein condensates into multiphase architectures. Proc Natl Acad Sci U S A. 2022;119(26):e2119800119. https://doi.org/10.1073/pnas.2119800119 PMID: 35727989

75. Robustelli P, Piana S, Shaw DE. Mechanism of coupled folding-upon-binding of an intrinsically disordered protein. J Am Chem Soc. 2020;142(25):11092–101. https://doi.org/10.1021/jacs.0c03217 PMID: 32323533